Available online at www.sciencedirect.com
ScienceDirect
Journal of Power Sources 178 (2008) 422–433
JOURNAL OF POWER SOURCES
www.elsevier.com/locate/jpowsour

Local structure and composition studies of $Li_{1.2}Ni_{0.2}Mn_{0.6}O_2$ by analytical electron microscopy

C.H. Lei [a], J. Bareño [a], J.G. Wen [a], I. Petrov [a], S.-H. Kang [b], D.P. Abraham [b,*]

[a] *Frederick Sietz Materials Research Laboratory, University of Illinois at Urbana-Champaign 104 S, Goodwin Avenue, Urbana, IL 61801, USA*
[b] *Chemical Sciences and Engineering Division, Argonne National Laboratory, 9700 South Cass Avenue, Argonne, IL 60439, USA*

Received 26 October 2007; accepted 13 November 2007
Available online 4 December 2007

Abstract

Positive electrodes for Li-ion batteries based on $Li[Li_{1/3-2x/3}Ni_xMn_{2/3-x/3}]O_2$ ($0 \le x \le 0.5$) compounds are of significant interest because of their ability to deliver reversible capacities exceeding 200 mAh g^{-1}. In this article we describe the examination of $Li_{1.2}Ni_{0.2}Mn_{0.6}O_2$ ($x = 0.2$ in $Li[Li_{1/3-2x/3}Ni_xMn_{2/3-x/3}]O_2$) samples by X-ray diffraction (XRD), high-resolution electron microscopy (HREM), scanning transmission electron microscopy (STEM), electron diffraction, X-ray energy dispersive spectroscopy (EDS), and electron energy loss spectroscopy (EELS). The studies were conducted on freshly prepared oxides, and on oxide electrodes that were electrochemically activated by cycling twice between 4.8 and 2.0 V vs. Li^+/Li. Rectangular and parallelogram shaped dot arrays with a spacing of 0.43 nm observed in HREM and STEM images along the [1 0 $\bar{1}$ 0] zone axis, as well as streaks at 1/3 n (1 1 $\bar{2}$ 0) (n = integer) positions in corresponding electron diffraction patterns, indicated ordering of Li-ions in the transition-metal (TM) (0 0 0 1) layers following several stacking sequences, bounded by stacking faults, along the c-axis. Chemical analysis by EDS and EELS showed that Mn, Ni and O were present in all portions of the samples examined; no evidence of elemental segregation was observed either within the grains or at grain boundaries. The Li ordering on TM planes was significantly weaker but still discernable upon electrochemical activation of the oxide samples.

Keywords: Electron microscopy; Lithium ordering; Plane stacking; Composition analysis

1. Introduction

The growth of the lithium-ion battery market has been fueled by the ever increasing demand for energy storage. The high energy and power densities of rechargeable lithium-ion cells have made them attractive for a wide range of applications, from portable electronics to hybrid electric vehicles [1,2]. Considerable materials research to further improve energy and power performance of these cells is being conducted at various laboratories worldwide. Of particular interest are the lithium nickel manganese oxide electrodes that can deliver reversible capacities exceeding 200 mAh g^{-1} over the 2.5–4.6 V potential window [3–8]. These $Li[Li_{1/3-2x/3}Ni_xMn_{2/3-x/3}]O_2$ ($0 \le x \le 0.5$) compounds have, in a general sense, a layered α-$NaFeO_2$-type structure ($R\bar{3}m$ symmetry) in which the Na sites are occupied by Li and the Fe sites are occupied by Li and both TM (Ni and Mn) ions. Fig. 1 shows a schematic of the atomic arrangement in the ideal $R\bar{3}m$ structure along the [1 1 $\bar{2}$ 0] and [1 0 $\bar{1}$ 0] zone axes, with the c-axis running vertical in the plane of the drawing. The structure can be viewed as a modified NaCl structure in which close-packed oxygen planes separate the alternating lithium layers and TM-rich layers. The nickel content in these compounds ranges from $x = 0$ in $Li[Li_{1/3}Mn_{2/3}]O_2$ (or Li_2MnO_3) to $x = 0.5$ in $Li[Ni_{0.5}Mn_{0.5}]O_2$.

The structure of compounds in the $Li[Li_{1/3-2x/3}Ni_xMn_{2/3-x/3}]O_2$ series has been examined by various computational and experimental methods [9–14]. X-ray absorption spectroscopy (XAS) data showed that the average valences for Ni and Mn ions in these compounds are +2 and +4, respectively [13]. From X-ray diffraction studies, Lu et al. suggested that, for compositions $0 \le x \le 1/3$, Li, Mn and Ni ions are ordered in the transition-metal layer on a $\sqrt{3} \times \sqrt{3}$ super-

* Corresponding author. Tel.: +1 630 252 4332; fax: +1 630 972 4406.
E-mail address: abraham@cmt.anl.gov (D.P. Abraham).

0378-7753/$ – see front matter © 2007 Elsevier B.V. All rights reserved.
doi:10.1016/j.jpowsour.2007.11.077

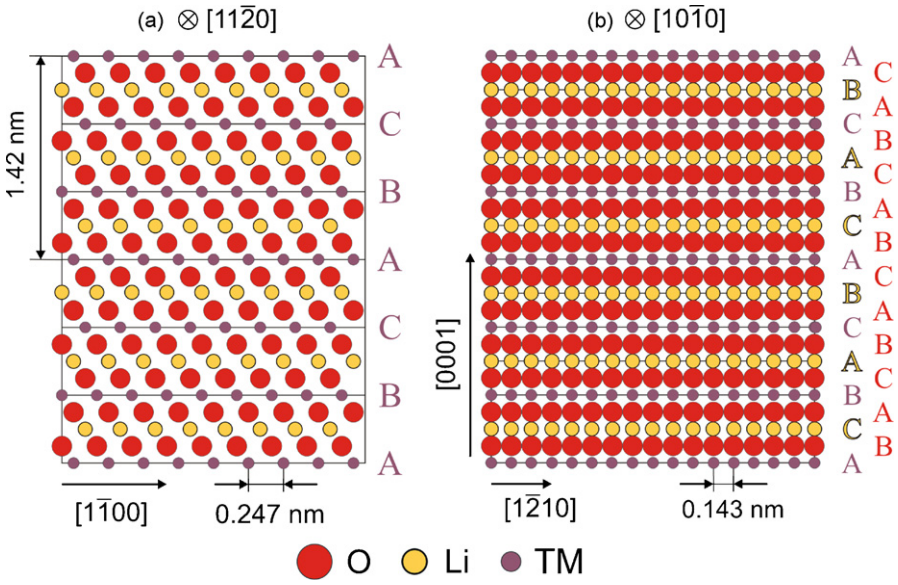

Fig. 1. Cross-sectional schematic views of the ideal $R\bar{3}m$ structure projected along the (a) [1 1 $\bar{2}$ 0] and (b) [1 0 $\bar{1}$ 0] zone axes. The FCC stacking sequence of transition-metal (TM) planes and of all planes is marked on panels (a) and (b), respectively. The *c*-axis length and spacing between projected atomic columns are shown in the figure.

structure (in the hexagonal description) [15]. Similar in-plane $\sqrt{3} \times \sqrt{3}$ ordering was also found in the transition-metal layers of $Li[Li_{1/9}Ni_{1/3}Mn_{5/9}]O_2$ and Li_2MnO_3 [16]. Furthermore, the ordered transition-metal layers showed particular stacking sequences along the c_{hex} axis; mostly $P3_112$ stacking with some abnormal $C2/m$ stacking, and two or three different $C2/m$ stacking variants [16].

Lu et al. reported that ordering is not expected in $Li[Ni_{0.5}Mn_{0.5}]O_2$ because their X-ray diffraction data showed little indication of the $\sqrt{3} \times \sqrt{3}$ superstructure peaks for this composition [15]. However, electron diffraction data and diffraction simulation studies on $Li[Ni_{0.5}Mn_{0.5}]O_2$ by Meng et al. [16–18] have revealed the existence of in-plane ordering in the transition-metal layers, which contain a considerable number of Li-ions as a result of Li and Ni interlayer exchange. Their data indicate that Li, Mn and Ni ions are not distributed randomly in the transition-metal layers but order and form two sublattices with significantly different occupations. First-principles computation and ^{6}Li magic-angle spinning (MAS) nuclear magnetic resonance (NMR) analysis on $Li[Ni_{0.5}Mn_{0.5}]O_2$ have revealed strong ordering interactions between Li^+ and Mn^{+4} ions, and Ni^{+2} and Mn^{+4} ions [19]. In addition, the MAS-NMR data showed that the Li^+ ions have a much higher probability of being surrounded by six Mn^{+4} ions than would be found in a random solid solution. Because the cation configuration $[LiMn_6]$ is the building block for Li_2MnO_3, the $Li[Li_{1/3-2x/3}Ni_xMn_{2/3-x/3}]O_2$ composition has been rewritten in two-component rocksalt notation as $yLi_2MnO_3 \cdot (1-y)Li[Ni_{0.5}Mn_{0.5}]O_2$ (allowing for some cation segregation and disorder), where $y = (1-2x)/(1+x)$ [20–22]. That is, the $Li[Li_{1/3-2x/3}Ni_xMn_{2/3-x/3}]O_2$ compound is described as a composite structure of ordered or partially disordered Li_2MnO_3 domains intergrown and integrated with the $Li[Ni_{0.5}Mn_{0.5}]O_2$ structure [21]. This two-component notation allows one to follow electrochemical insertion/extraction processes on a Li_2MnO_3–$LiMO_2$–MO_2 (M = Ni, Mn) ternary phase diagram [22].

Armstrong et al. [23] investigated the structure of $Li_{1.2}Ni_{0.2}Mn_{0.6}O_2$ by neutron diffraction analysis; this composition corresponds to $x = 0.2$ in $Li[Li_{1/3-2x/3}Ni_xMn_{2/3-x/3}]O_2$, or $0.5\ Li_2MnO_3 \cdot 0.5Li[Ni_{0.5}Mn_{0.5}]O_2$ in the two-component rocksalt notation. Rietveld refinement of their data revealed 1.6% Ni and 98.4% Li on the octahedral sites of the Li layers, i.e. the degree of Ni and Li interlayer mixing is far smaller than the 9–12% reported for a pure $Li[Ni_{0.5}Mn_{0.5}]O_2$; the Mn, Ni, and Li occupancy of octahedral sites of the transition-metal layers was determined to be 60%, 17.2% and 22.8%, respectively. Oxygen evolution was observed by differential electrochemical mass spectrometry when $Li_{1.2}Ni_{0.2}Mn_{0.6}O_2$ was charged above 4.5 V. Refinement of neutron diffraction data from a sample charged to 4.8 V indicated that oxygen loss from the surface was accompanied by a diffusion of transition-metal ions from the surface to the bulk where they occupy vacancies created by Li removed from the transition-metal planes.

In this article we describe the examination of $Li_{1.2}Ni_{0.2}Mn_{0.6}O_2$ samples by analytical electron microscopy. Both freshly prepared samples, and samples that were electrochemically activated at 4.8 V then discharged to 2 V, were examined. A combination of techniques, including high-resolution electron microscopy (HREM), high-angle annular dark-field imaging in scanning transmission electron microscopy (HAADF-STEM), and selected-area electron diffraction were used to examine the sample crystal structures. In-plane ordering of Li, Mn and Ni in the transition-metal rich layers and possible stacking sequences of the in-plane ordered layers are discussed. X-ray energy dispersive spectroscopy (EDS) and electron energy loss spectroscopy (EELS) were used to probe sample compositions on nanosized scales; these data are used to examine structural and compositional

variations in $Li_{1.2}Ni_{0.2}Mn_{0.6}O_2$ with $\lesssim$2 Å lateral spatial resolution.

2. Experimental

2.1. Materials synthesis, X-ray diffraction, and electrochemistry

The $Li_{1.2}Ni_{0.2}Mn_{0.6}O_2$ compound was synthesized from mixed nickel–manganese carbonate precursors, prepared by a coprecipitation method, and lithium carbonate. First, a 0.2 M aqueous solution of nickel sulfate and manganese sulfate (Ni/Mn = 1:3) was added to a 1 M, equivolume, aqueous solution of sodium hydrogen carbonate, from which green precipitates formed immediately; the mixed solution was aged for 24 h. The coprecipitation and aging procedures were carried out under constant stirring (250 rpm) at 50 °C. The $(Ni_{0.25}Mn_{0.75})CO_3$ precipitate was filtered, washed, dried at 108 °C, and thereafter intimately mixed with Li_2CO_3. The $Li_{1.2}Ni_{0.2}Mn_{0.6}O_2$ product was obtained by firing the mixed precursors at 900 °C for 6 h in air. Powder X-ray diffraction patterns of the synthesized material were collected on a Siemens D5000 diffractometer (Cu Kα radiation) between 10 and 80° 2θ at a scan rate of 0.25° 2θ/min.

The $Li_{1.2}Ni_{0.2}Mn_{0.6}O_2$ material was electrochemically activated in 2032-type coin cells containing a Li counter electrode. The positive electrode was prepared by coating a mixture of 84 wt% oxide, 4 wt% SFG-6 graphite, 4 wt% acetylene black, and 8 wt% polyvinylidene difluoride (PVdF) on a 30-μm-thick Al foil. The electrolyte was 1 M $LiPF_6$ in an ethylene carbonate:diethyl carbonate (EC:DEC) (1:1, w/w) solvent. A 25 μm thick Celgard 2325 separator provided electronic isolation between the electrodes, while allowing the conduction of lithium ions. The electrochemical activation of the oxide was conducted by cycling the cells twice between 2.0 and 4.8 V, with a current density of 0.1 mA cm^{-2}, at room temperature.

2.2. Analytical electron microscopy

The transmission electron microscopy (TEM) samples were prepared in several steps which are as follows: (1) a 3-mm disk was punched out from the composite electrode, (2) the disk was then glued on to a Cu-ring, (3) the Al current collector was then gently removed leaving only the electrode coating on the Cu-ring, (4) the oxide-bearing disk was then subjected to low-angle (6°) Ar-ion milling at 5 kV from both sides for 30 min followed by 3-kV milling to perforation (~30 min); the sample was cooled with liquid nitrogen during ion milling. This sample preparation protocol produced large, thin areas that contained many oxide particles suitable for crystal structure examination by HREM and composition study by EELS.

Lattice-resolution transmission electron microscopy and selected-area electron diffraction (SAED) studies were carried out at 200 keV with a JEOL 2010LaB6, while HAADF-STEM images were acquired using a JEOL 2200FS instrument equipped with a probe aberration corrector (CEOS GmbH, Heidelberg, Germany). The samples were tilted in the microscopes to examine the crystal structure along various zone axes. The point-to-point resolution of the JEOL 2010LaB6 is 0.22 nm in the TEM mode, while the resolution of the JEOL 2200FS is nominally 0.1 nm in the high-angle annular dark-field (HAADF) mode. Compositional analyses of particles were conducted using JEOL2010F instruments with an energy dispersive spectrometer equipped with an Oxford INCA thin-window Si(Li) detector and a Gatan Image Filter 2001 that filtered both images and diffraction patterns and served as an electron energy loss spectrometer. Both EDS and EELS data were collected in the STEM mode with a probe size that was $\leq$1 nm.

3. Results

3.1. As-synthesized samples

3.1.1. X-ray diffraction

Fig. 2 shows a powder X-ray diffraction pattern from as-synthesized oxide powders. Most of the diffraction peaks in the pattern can be indexed based on the α-$NaFeO_2$ ($R\bar{3}m$) structure, with lattice constants $a = 0.2854$ nm and $c = 1.4225$ nm in the hexagonal representation. In addition to the reflections derived from the $R\bar{3}m$ structure, a set of small, relatively broad peaks are visible in the range from $2\theta = 20°$ to 25°. These peaks are characteristic of cation ordering in the transition-metal TM layers, as occurs between the lithium and manganese ions in Li_2MnO_3, where a hexagonal (flower-like) arrangement of Li-ions in the TM-planes reduces the symmetry of the system to (monoclinic) $C2/m$ [24]. Accordingly, the extra peaks in this 2θ range can be indexed to the (0 2 0), (1 1 0), and (1 1 $\bar{1}$) lattice planes with monoclinic ($C2/m$) symmetry as in the Li_2MnO_3 unit cell.

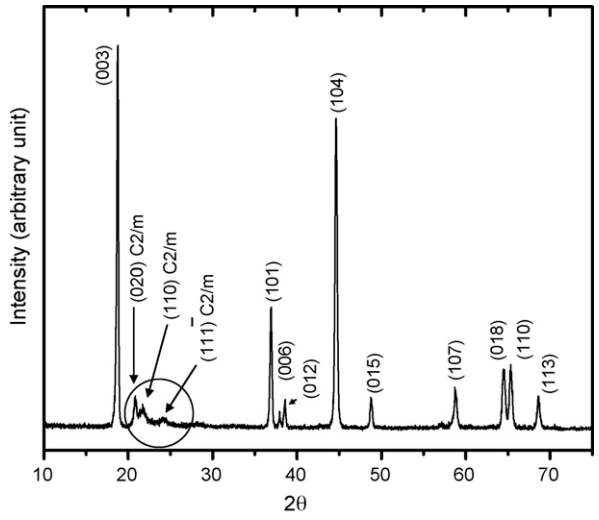

Fig. 2. XRD powder pattern of an-synthesized $Li(Li_{0.2}Ni_{0.2}Mn_{0.6})O_2$ sample. The pattern has been indexed with respect to the $R\bar{3}m$ structure, with lattice constants $a = 0.2854$ nm and $c = 1.4225$ nm, with additional weaker peaks in the range $20° \leq 2\theta \leq 25°$.

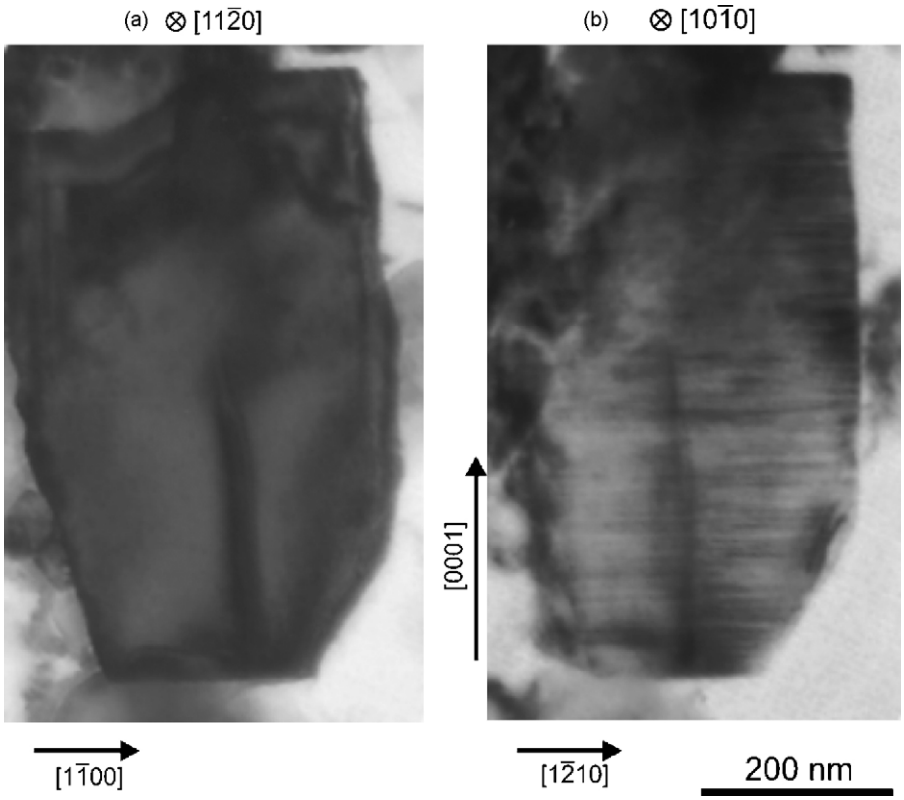

Fig. 3. Low-magnification TEM image of a $Li(Li_{0.2}Ni_{0.2}Mn_{0.6})O_2$ grain in the as-synthesized sample, recorded along (a) the [1 1 $\bar{2}$ 0] and (b) the [1 0 $\bar{1}$ 0] zone axes. A distinct fringe contrast is present in the [1 0 $\bar{1}$ 0] projection, arising from an internal platelet structure in the grain.

3.1.2. Electron microscopy—structure analysis

Figs. 3–6 show electron microscopy data from the as-synthesized samples. Images and diffraction data were obtained from several grains in the sample. The data from various grains were very similar; therefore, only representative data are shown in this article.

Fig. 3 contains TEM bright field images taken along the [1 1 $\bar{2}$ 0] and [1 0 $\bar{1}$ 0] directions of a whole oxide grain with the *c*-axis running vertically in the plane of the picture, as marked in the figure. The grain shows no particular contrast variation when imaged along the [1 1 $\bar{2}$ 0] zone axis (Fig. 3a) other than a central dark stripe in the bottom half of the panel, probably due to an antiphase boundary in the grain. Imaging along [1 0 $\bar{1}$ 0] (Fig. 3b) reveals a striped bright and dark diffraction contrast running perpendicular to the [0 0 0 1] direction, which indicates the presence of very thin "platelets" or stacking faults along the *c*-axis. Higher magnification images showed that several of these "platelets" had a width in the range of 1–5 nm. This stripe contrast variation disappears when the grain is rotated around the *c*-axis away from the [1 0 $\bar{1}$ 0] direction.

Selected-area electron diffraction (SAED) provides complementary information to bright field images. Fig. 4a and b show the corresponding electron diffraction patterns obtained along the [1 1 $\bar{2}$ 0] zone axis and along the [1 0 $\bar{1}$ 0] zone axis, respectively. Along the [1 1 $\bar{2}$ 0] zone axis the diffraction pattern consists only of sharp spots; all reflections can be indexed based on the $R\bar{3}m$ structure. The [1 0 $\bar{1}$ 0] zone axis diffraction pattern, however, in addition to sharp reflections from the $R\bar{3}m$ structure, exhibits diffuse streaks along (0 0 0 1), perpendicular to the reciprocal vector $g = (1\,1\,\bar{2}\,0)$, and at $n/3(1\,1\,\bar{2}\,0)$ (n = integer) positions. The inset in Fig. 4b is a plot of the diffraction pattern intensity, integrated in the area marked by the dotted box in the picture, as a function of position along the $(1\,1\,\bar{2}\,0)$ reciprocal vector. A least squares fit of four Lorentzian peaks to the spectrum revealed that the intensity of the streaks, measured as the area under the corresponding peaks, is $\simeq$ 50% that of the $R\bar{3}m$ spots.

The 1/3 $(1\,1\,\bar{2}\,0)$ spacing of the streaks indicates a periodicity of $3 \times d\ [1\,1\,\bar{2}\,0] \simeq 0.43$ nm, which corresponds to an XRD reflection at 22° that is in the range of the extra peaks present in Fig. 2. The presence of streaks indicates the existence of platelets along the *c*-axis, while the sharpness of the streaks is related to platelet thickness; weak spots, occasionally observed superposed on the streaks, are indicative of thicker platelets. In other words, the streaks in the SAED patterns can be viewed as the reciprocal space counterparts (Fourier transforms) of the thin platelets observed in Fig. 3b. Further evidence of this interpretation is provided below.

Fig. 5a and b show HREM images obtained along the [1 1 $\bar{2}$ 0] zone axis and along the [1 0 $\bar{1}$ 0] zone axis, respectively. HREM images are formed by recombining the transmitted beam with multiple diffracted beams in a given zone axis. The phase interference between these beams results in a periodic fringe contrast representative of different atomic columns, which allows the unique determination of lattice spacings and angular symmetries within the sample.

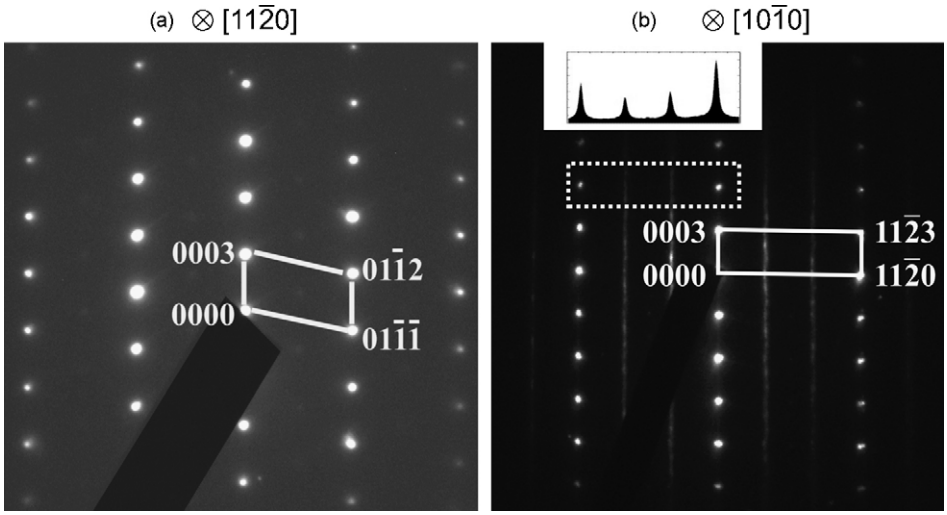

Fig. 4. SAED patterns from a sample of as-synthesized $Li(Li_{0.2}Ni_{0.2}Mn_{0.6})O_2$, recorded in the (a) [1 1 $\bar{2}$ 0] and (b) [1 0 $\bar{1}$ 0] zone axes. The [1 1 $\bar{2}$ 0] zone axis pattern shows only the expected reflections from the $R\bar{3}m$ structure, while the [1 0 $\bar{1}$ 0] zone axis pattern shows additional streaks at the $n/3(1\,1\,\bar{2}\,0)$ positions.

The lattice image along the [1 1 $\bar{2}$ 0] zone axis (Fig. 5a) is consistent with the [1 1 $\bar{2}$ 0] projection of the $R\bar{3}m$ structure. The 0.247 nm spacing between the white spots is the expected spacing between atomic columns (see Fig. 1a), while the interplanar spacing of 0.474 nm is the expected spacing between the TM planes (or the Li planes). As in the corresponding diffraction pattern given in Fig. 4a, no evidence of additional ordering within the basal planes is present in this image.

Along the [1 0 $\bar{1}$ 0] zone axis, the closest distance between two atomic columns in the (0 0 0 1) planes of a stoichiometric $R\bar{3}m$ compound is 0.143 nm, which is smaller than the resolution of the TEM instrument used to produce these images. Consequently, HREM images of the (0 0 0 1) planes are expected to show only a continuous lattice fringe pattern along this zone axis. Fig. 5b, however, shows a sharp dot pattern. The distance between two closest dots within the (0 0 0 1) plane is $\simeq$0.43 nm, which is three times the projected distance between the closest atomic columns, corresponding to the 1/3 (1 1 $\bar{2}$ 0) spacing of the SAED streaks. Close examination of the dot array reveals two types of meshes, rectangular (R) and parallelogram (P) shaped, present at different locations in the image. The P meshes present a relative shift between successive layers of 1/3 of the neighboring dot distance within the plane, corresponding to the closest distance between two atomic columns along the [1 0 $\bar{1}$ 0] projection of the $R\bar{3}m$ structure (0.143 nm), as indicated previously. These meshes are typically between 2 and 10 layers tall ($\simeq$1–5 nm, in agreement with the platelets visible in Fig. 3b) and span the whole field of view in the horizontal direction. The different meshes indicate different stacking sequences along the *c*-axis, succeeding each other in a relatively random fashion. A few layers at the transition zone between some of the R and P meshes do not show clear

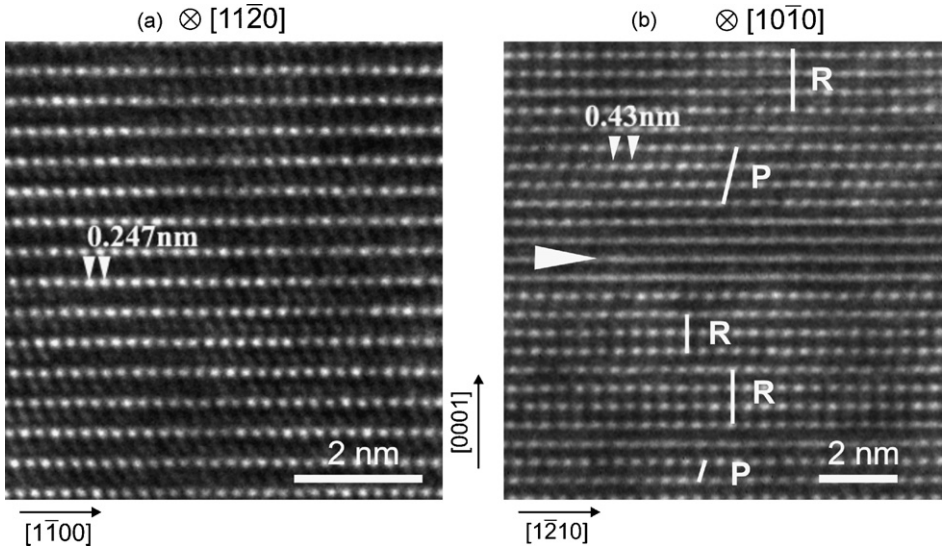

Fig. 5. HREM images of an as-synthesized $Li(Li_{0.2}Ni_{0.2}Mn_{0.6})O_2$ sample, recoded along the (a) [1 1 $\bar{2}$ 0] and (b) [1 0 $\bar{1}$ 0] zone axes. The atomic columns visible in the [1 1 $\bar{2}$ 0] projection correspond with the expected projection of the TM planes in the $R\bar{3}m$ structure, while the [1 0 $\bar{1}$ 0] projection shows an additional 0.43 nm periodicity that is indicative of Li-cation ordering within the TM planes. Different meshes with rectangular (R) and parallelogram (P) symmetry are marked in (b).

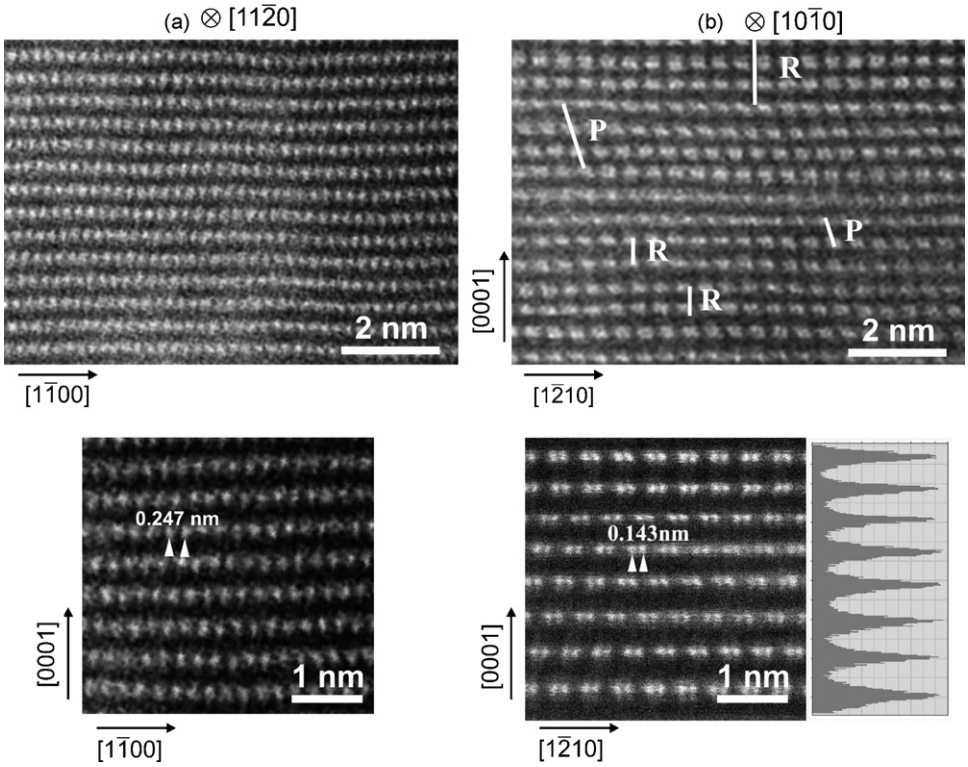

Fig. 6. High-resolution aberration-corrected HAADF (Z-contrast) images of the as-synthesized $Li(Li_{0.2}Ni_{0.2}Mn_{0.6})O_2$ sample, recorded along the (a) [1 1 $\bar{2}$ 0] and (b) [1 0 $\bar{1}$ 0] zone axes; the pictures in the lower half of each panel are higher magnification details of selected areas in the images directly above them. The inset in panel (b) is a plot of the intensity (horizontal axis) of the high-magnification image, integrated along the [1 $\bar{2}$ 1 0] direction, as a function of position along [0 0 0 1] (vertical axis). The periodicities expected from the projection of the $R\bar{3}m$ structure are the only ones present in the [1 1 $\bar{2}$ 0] zone axis image, while the [1 0 $\bar{1}$ 0] image shows an additional 0.43 nm periodicity that forms different meshes with rectangular (R) and parallelogram (P) periodicity along the image.

dot contrast in local areas, as indicated by the white arrow in Fig. 5b.

As mentioned in Section 1, Rietveld analysis of neutron diffraction data obtained on a comparable sample showed that the TM layer composition was $[Li_{0.228}Ni_{0.172}Mn_{0.6}]$ and that the Li layer composition was $Li_{0.984}Ni_{0.016}$. The amount of Li present in the TM layers is very close to the fraction of dark area within the dot arrays in Fig. 5b. Qualitatively, one out of three atomic columns in the bright (0 0 0 1) planes is dark. Thus, the HREM pictures presented in Fig. 5 can be interpreted as showing the (bright) TM (0 0 0 1) planes, separated by three (dark, O–Li–O) planes; and the $3 \times [1\,1\,\bar{2}\,0]$ periodicity is consistent with a $\sqrt{3} \times \sqrt{3}$ Li-cation ordering in the TM-planes.

In order to confirm this interpretation, we obtained aberration-corrected HAADF images (also called STEM or Z-contrast images) of the sample. HAADF images are formed by scanning a finely focused electron probe over a specimen in a two-dimensional raster. Electrons reflected by the specimen at high angles are collected at an annular detector (angular range >50 mrad), amplified, and used to modulate the brightness of the displayed image. Interpretation of STEM images is simpler because the intensity in each pixel is proportional

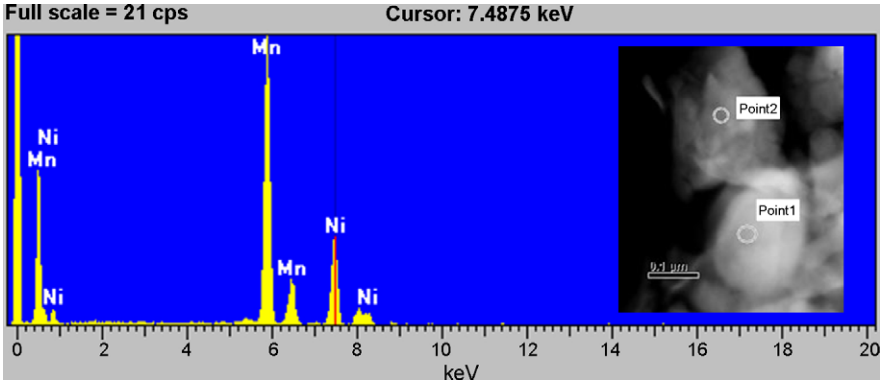

Fig. 7. Representative (STEM, dark-field mode) EDS spectrum acquired from an as-synthesized $Li(Li_{0.2}Ni_{0.2}Mn_{0.6})O_2$ sample, showing the presence of both Mn and Ni. The inset shows a TEM picture; typical locations for EDS spectra acquisition are marked.

to the incoherent scattering at each beam position, which in turn is a function of both the average atomic number Z of the projected atomic column and the local specimen thickness. Thus, TM-rich atomic columns are expected to appear significantly brighter in HAADF imaging than either Li-rich or O columns.

Fig. 6a and b show two HAADF images of the same area of the sample, recorded along the [1 1 $\bar{2}$ 0] zone axis and along the [1 0 $\bar{1}$ 0] zone axis, respectively; the lower picture in each panel shows a higher magnification version of the image directly above it. The aberration-corrected HAADF image in the [1 1 $\bar{2}$ 0] zone axis exhibits a series of bright horizontal rows, which are associated with the (high Z) TM-rich layers, separated by a dark area attributed to the (lower Z) Li-rich and O layers. The measured separation between the bright rows is 0.47 nm, which corresponds to the expected distance between TM layers, and each row presents a uniform spot pattern with spacing of 0.247 nm, corresponding to the periodicity of the TM columns (see Fig. 1a). A slight gradient of the average intensity is seen in the micrograph with brightness decreasing from left to right corresponding to a weak thickness variation across the sample. The intensity of the bright spots in the [1 1 $\bar{2}$ 0] image is uniform for any given thickness, indicating a constant average atomic number of the columns in this projection.

The aberration-corrected HAADF image along the [1 0 $\bar{1}$ 0] zone axis (Fig. 6b) shows distinct R and P dot patterns with a separation of 0.43 nm, in accordance to the HREM picture in Fig. 5b. Additionally, the higher magnification micrograph shows the 0.143 nm spacing between the TM columns (see Fig. 1b). The pattern of two bright columns followed by a dark column, which is most pronounced in the top and bottom rows in the figure while smeared out in the middle rows, is a direct consequence of the atomic arrangement in the plane, following a sequence of two TM-rich columns (higher Z, brighter) and one Li-rich column (lower Z, darker). The integrated intensity along the rows (shown on the right side of the lower image), is uniform from the top to the bottom of the picture, indicating that the average atomic number is the same in every TM-plane, regardless of the differences in contrast between the dark and bight columns. We can conclude that the smearing out of the contrast in some rows, observed in the aberration-corrected HAADF and HREM [10$\bar{1}$0] images, is not due to variations in the Li content from row to row (between TM close-packed planes) but results, probably, from the presence of a fault in the Li ordering within the TM plane within the thickness of the TEM sample that produces an overlap of both P and R domains.

In summary, high-resolution aberration-corrected HAADF imaging provides confirmation of the interpretation of HREM contrast modulations as arising from Li-ordering in the TM-rich (0 0 0 1) planes. More details about this ordering will be presented in Section 4.

3.1.3. Electron microscopy—chemical analysis

EDS is based on the energy distribution analysis of characteristic X-ray photons generated when high-energy incident electrons interact with a specimen exciting the inner-shell electrons of the specimen atoms. EELS is based on the energy distribution analysis of high-energy electrons that have been inelastically scattered by the specimen. Incident high-energy electrons lose energy by excitation of discrete inner-shell electrons in the specimen atoms to empty states above the Fermi level, resulting in energy loss spectra (also termed edge profiles) characteristic of each atomic species. For example, Mn and Ni $L_{2,3}$ edges are the result of electron transitions from 2p to unfilled 3d levels, while the O K edge arises from electron transitions between the 1s and unoccupied 2p levels of the oxygen atom. Both EDS and EELS data were obtained on our samples in the STEM mode because the small probe size ($\lesssim$1 nm) allowed compositional analysis to be performed with nanometer resolution.

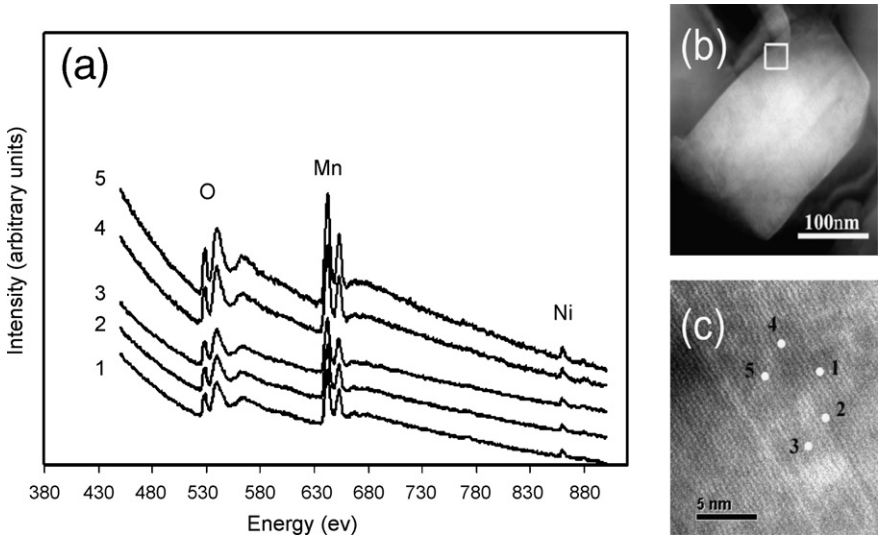

Fig. 8. (a) Representative EELS spectra from a grain, shown in (b), in an as-synthesized $Li(Li_{0.2}Ni_{0.2}Mn_{0.6})O_2$ sample that showed a clear high-resolution HAADF image along the [1 0 $\bar{1}$ 0] zone axis. The probing positions, selected from areas displaying different atomic meshes, are indicated in (c), which is a local enlargement of the area marked by a white box in (b).

EDS spectra were acquired at several randomly picked locations in the sample, both within grains and at grain boundaries, using a 1 nm probe size. The corresponding analysis volume is estimated to be $\simeq$10 nm^3 due to beam spreading within the sample. Fig. 7 is a representative EDS spectrum showing Mn and Ni peaks, both of which were present at every sample location probed.

EELS spectra, both single-point data and line scans, were collected from the samples using a probe size between 0.2 and 0.5 nm. The corresponding analysis volume is estimated to be less than 10 nm^3. Most data were obtained along the [1 0 $\bar{1}$ 0] zone axes; some data were also collected along the [1 1 $\bar{2}$ 0] axis. Fig. 8 shows a series of EELS spectra from a fresh grain that showed clear high-resolution HAADF image along the [1 0 $\bar{1}$ 0] zone axis (side panel), at several probing positions in R and P meshes. Although there are some intensity variations from location to location, the presence of Mn, Ni and O are evident in all the spectra. In addition, the shape, position, and intensity of our O K-edge and transition-metal (Mn $L_{2,3}$, Ni$L_{2,3}$)-edge data are consistent with those reported by Miao et al. from EELS studies, and by Yoon et al. from soft X-ray absorption studies, on $Li_x[Ni_{0.5}Mn_{0.5}]O_2$ and $Li_x[Ni_{1/3}Co_{1/3}Mn_{1/3}]O_2$ samples [25–27].

In addition to the EDS and EELS data, composition variations along the *c*-axis were studied by summing the HAADF intensities along both [1 1 $\bar{2}$ 0] and [1 $\bar{1}$ 0 0] zone axis images; an example is shown in Fig. 6b (right side, lower image). Careful examination of these data showed no significant intensity differences between the various basal planes, which indicated that the basal plane composition was uniform throughout the sample.

In summary, a combination of HAADF, EDS, and EELS analyses showed a homogeneous overall composition along the *c*-axis. In-plane compositional variations, if any, are limited to domain sizes smaller than the probe volume $\simeq$10 nm^3. Furthermore, preferential segregation of any atomic species either within grains or at grain boundaries was not observed.

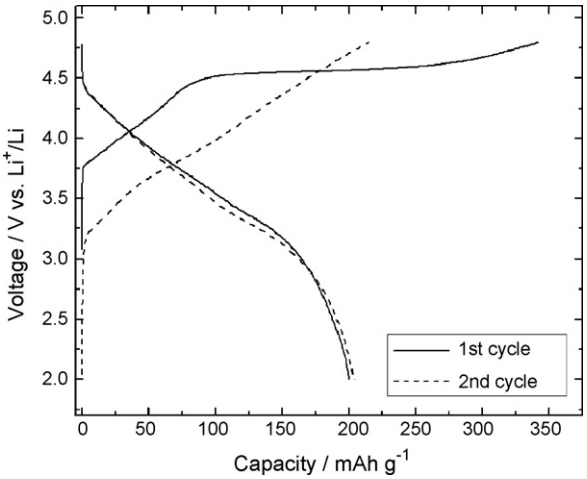

Fig. 9. Charge–discharge cycling data from a Li($Li_{0.2}Ni_{0.2}Mn_{0.6}$)O_2/Li cell showing a $\simeq$4.5 V plateau during the first charge. Note that the plateau is not observed during the second charge.

3.2. Electrochemically activated samples

3.2.1. Electrochemistry

Fig. 9 shows charge–discharge cycling data from a $Li_{1.2}Ni_{0.2}Mn_{0.6}O_2$//Li cell; the data are in accord with those reported previously on other $Li[Li_{1/3-2x/3}Ni_xMn_{2/3-x/3}]O_2$ electrodes [6,20–23,28,29]. During the first charge cycle, the voltage increases monotonically until ~4.5 V corresponding to the oxidation of Ni^{+2} to Ni^{+4}. The long plateau observed, starting at ~4.5 V, has been attributed to simultaneous removal of lithium and oxygen from the oxide material [23]. The 200 mAh g^{-1} first cycle discharge capacity is much larger than the 128 mAh g^{-1} value calculated from the oxide's transition-metal content. Fig. 9 shows that the ~4.5 V plateau is not seen during the second charge. Other data have shown that the plateau is not observed after the first charge cycle; moreover, the cells display good cycling stability in spite of the high-upper cut-off voltage [30].

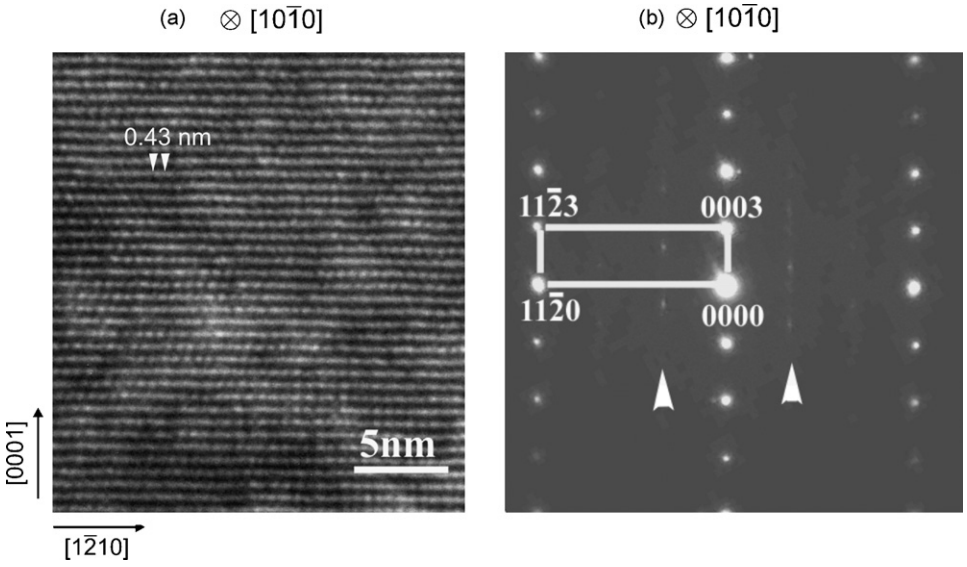

Fig. 10. (a) HREM image and (b) SAED pattern of an electrochemically activated Li($Li_{0.2}Ni_{0.2}Mn_{0.6}$)O_2 sample, recorded along the [1 0 $\bar{1}$ 0] zone axis. Although still visible, the Li-cation ordering in the TM planes is much weaker than in the as-synthesized sample.

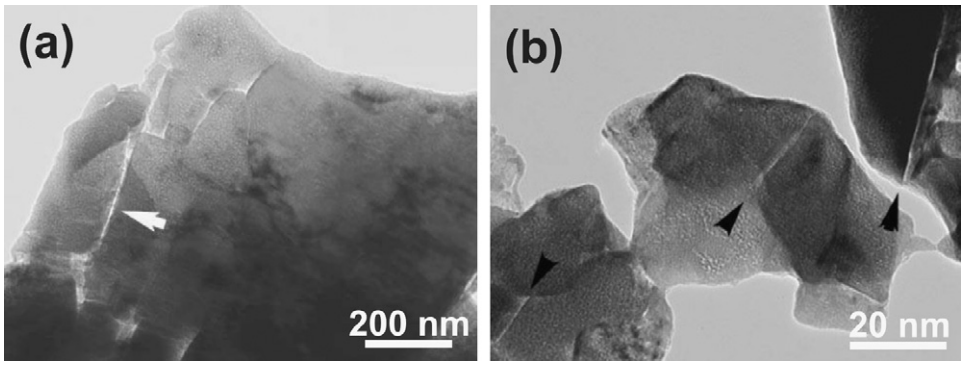

Fig. 11. Low magnification TEM images of an electrochemically activated $Li(Li_{0.2}Ni_{0.2}Mn_{0.6})O_2$ sample showing cracks, presumably due to loss of material during electrochemical charging above 4.5 V. The cracks, which are marked by arrows in the figure, were usually observed along (0 0 0 1) planes.

X-ray diffraction patterns (not included) obtained on the cycled samples (discharged to 2.0 V) showed very weak peaks in the 20–25° 2θ range; i.e., the intensity of these peaks was significantly diminished by the high-voltage cycling, in agreement with previous reports [23,30].

3.2.2. Electron microscopy—structure analysis

Fig. 10a and b show a HREM image and an electron diffraction pattern, along the [1 0 $\bar{1}$ 0] zone axis, obtained on an electrochemically activated sample that was discharged to 2.0 V. In addition to reflections from the $R\bar{3}m$ structure, the electron diffraction pattern shows weak spots and some diffuse streaks at $n/3$ (1 1 $\bar{2}$ 0) positions. Following the same procedure used for Fig. 4b, we found that the intensity of these streaks is ≃5% that of the $R\bar{3}m$ spots. Although one order of magnitude weaker than in the as-synthesized sample, the presence of these streaks suggests residual Li ordering in the TM-rich layers of the electrochemically activated sample.

Only fringe patterns were observed in most HREM images obtained on the sample; however, dot arrays were also observed locally, as shown in Fig. 10a. A comparison of Figs. 10a and 5b shows significant differences in the sharpness and contrast of the dot arrays, indicating that electrochemical activation of the samples significantly reduces the ordering of Li cations in the TM (0 0 0 1) planes. Furthermore, low-magnification TEM images (Fig. 11) showed several microscopic cracks in the activated sample. These cracks are predominantly observed on (0 0 0 1) planes, and are consistent with loss of material from the sample. EELS and EDS STEM analysis of the electrochemically activated samples showed a uniform distribution of Ni and Mn, similar to those of the fresh sample results described above.

4. Discussion

Fig. 12a and b show a schematic diagram of the TM (0 0 0 1) plane, with the composition $Li_{0.22}Ni_{0.17}Mn_{0.61}O_2$, which is a hexagonal plane with a 0.2854 nm lattice constant. Two different kinds of atomic sites are present in this plane, α- and β-sites, indicated respectively by circles (yellow, blue, and green) and line crossings in Fig. 12a and b. The α-sites, where Li substitution for Mn is possible, form a $\sqrt{3} \times \sqrt{3}$ sublattice (marked by a discontinuous green line in Fig. 12a and b) in which each α-site is surrounded by a hexagon of β-sites. In the ideal Li_2MnO_3 $\{Li[Li_{1/3}Mn_{2/3}]O_2\}$ structure, all of the α-sites are occupied by Li substitutionals and all of the β-sites are occupied by Mn atoms. This configuration results in the $LiMn_6$ local environment reported from NMR measurements [16,18,24,28].

As Ni is added to the structure, it substitutes for Li and Mn atoms in α- and β-sites in a 2:1 ratio, according to $Li[Li_{1/3-2x/3}Ni_xMn_{2/3-x/3}]O_2$ stoichiometry. In $Li_{1.2}Ni_{0.2}Mn_{0.6}O_2$ ($x = 0.2$) 40% of the α-sites and 10% of the β-sites are occupied by Ni. Ni substitution for Li in the α-sublattice preserves the $LiMn_6$ coordination, while Ni substitution for Mn in the β-sublattice can induce other local configurations (such as $LiMn_5Ni$, reported by Bréger et al. [18]). Alternatively, Ni incorporation into the β-sublattice can also preserve $LiMn_6$ coordination if there is some degree of Ni-clustering in the α-sublattice. Thus, the possibility of Ni ordering within the α-sublattice needs to be considered.

Fig. 12a shows one possible arrangement where Ni atoms in the α-sublattice (blue circles) arrange in a 3×3 superlattice, leaving 2/3 of the α-sites occupied by Li (yellow circles); this configuration corresponds to a $Li_{0.22}Ni_{0.17}Mn_{0.61}O_2$ ($x = 1/6$) TM-plane composition. Fig. 12b shows the disordered counterpart of Fig. 12a, in which Ni and Li are randomly distributed in the α-sites (green circles) to an average 0.33 Ni occupation. In both cases 1/12 of β-sites is occupied by Ni (not shown).

Fig. 12c and d present two different [1 $\bar{1}$ 00] projections of the structure where, for clarity, only the TM planes are shown. Each TM (0 0 0 1) plane projects onto a row of atomic columns separated by 0.143 nm. This separation is below the TEM resolution of ≃2 Å and one should expect TM (0 0 0 1) planes to appear as continuous fringes in a HREM micrograph, although it is resolvable by aberration-corrected HAADF imaging as shown in Fig. 6b (lower panel). The $\sqrt{3} \times \sqrt{3}$ arrangement of the α-sublattice, if present, manifests itself in two distinct kinds of atomic columns: one containing ≃66% Li (green circles) and one devoid of Li (magenta circles), with the Li-containing column repeating every third position (0.43 nm periodicity). This periodicity corresponds well to the streaks at $n/3$ (1 1 $\bar{2}$ 0) positions (SAED patterns shown in Fig. 4b) and to the 0.43 nm periodicity along (0 0 0 1) planes in the [1 0 $\bar{1}$ 0] zone axis observed in both HREM (Fig. 5b) and aberration-corrected HAADF (Fig. 6b) images. This periodicity arises from the big difference in atomic numbers between Li atoms and Mn and

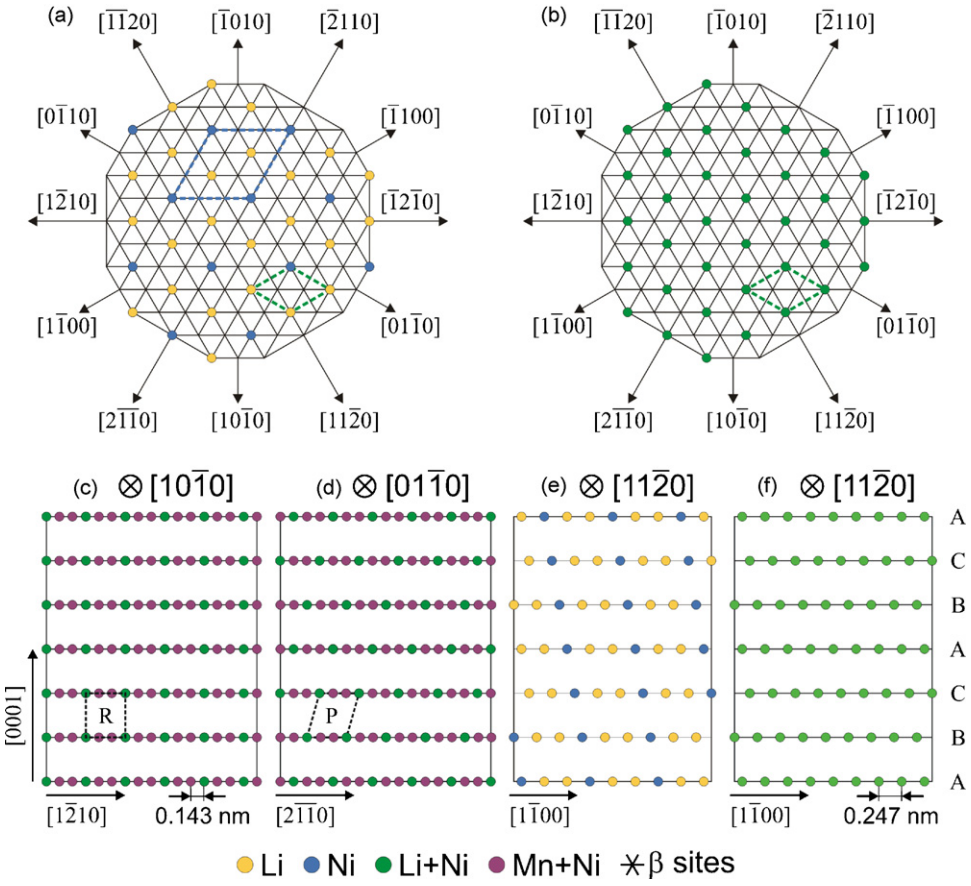

Fig. 12. (a and b) Plan views of a TM (0 0 0 1) plane in the ideal $Li(Li_{0.2}Ni_{0.2}Mn_{0.6})O_2$ structure showing in-plane ordering of Li cations. Yellow and blue circles mark the α-sites where Li substitution for TM atoms is possible, while thin line crossings represent β-sites. The α-sites form a $\sqrt{3} \times \sqrt{3}$ sublattice (marked with a discontinuous green line). Panel (a) shows a possible ordered arrangement where Li (yellow circles) and Ni (blue circles) atoms occupy the α-sites in a 3×3 superstructure (blue discontinuous line), while panel (b) the disordered counterpart of panel (a) in which both Ni and Li are randomly distributed in the α-sublattice to a 1/3 average Ni occupation (green circles). (c–f) Cross-sectional views of the TM (0 0 0 1) plane stacking sequence, assuming an in-plane slip vector $s = 1/3$ [$\bar{1}$ 0 1 0]. Panels (c) and (d) present two different projections along equivalent [1 0 $\bar{1}$ 0] zone axes. The α-sublattice projects as an array of Li/Ni-rich (green circles) and Mn-rich (magenta circles) atomic columns that, upon TM plane stacking, form rectangular (R, panel c) or parallelogram (P, panel d) shaped meshes when the zone axis is, respectively, parallel to or 60° rotated with respect to the in-plane component of the slip vector *s*. Panels (e) and (f) show, respectively, [1 1 $\bar{2}$ 0] zone axis projections of the ordered (panel a) and disordered (panel b) Ni configurations within the α-sublattice.

Ni atoms ($Z = 3$, 25, and 28, respectively). The Li in the TM layers causes a phase modulation of the electron beam because of the significantly different scattering abilities of the Li atoms and the transition-metal atoms. That is, the presence of Li in the TM (0 0 0 1) plane introduces a phase contrast that produces a dot pattern instead of the expected continuous fringe pattern in HRTEM images. The Li-rich columns are imaged directly as darker spots in the HAADF image. Thus, electron diffraction patterns, HRTEM and HAADF imaging provide complementary evidence of the presence of $\sqrt{3} \times \sqrt{3}$ superstructure in the fresh $Li_{1.2}Ni_{0.2}Mn_{0.6}O_2$ sample.

The TM (0 0 0 1) planes in the $R\bar{3}m$ structure follow an (FCC-like) ABC stacking sequence (see Fig. 1). The translation vector between two equivalent atoms in consecutive TM (0 0 0 1) planes has a 0.473 nm component along the *c*-axis and a $a/\sqrt{3} \simeq$ 0.165 nm component along the [1 0 $\bar{1}$ 0] direction. Two different kinds of meshes result when the structure is projected along one of six equivalent [1 $\bar{1}$ 0 0] axes. When the zone axis is parallel to the in-plane component of the translation vector (Fig. 12c) each TM atomic column sits directly above an equivalent column in the TM (0 0 0 1) plane below, resulting in a rectangular mesh (R). However, when the zone axis is ±60° rotated with respect to the in-plane component of the translation vector, each TM (0 0 0 1) plane appears to be displaced by one atomic column with respect to the TM (0 0 0 1) plane directly below (Fig. 12d), resulting in a parallelogram-shaped mesh (P) inclined at an angle of ≃73°. Both kinds of meshes are observed in [1 0 $\bar{1}$ 0] zone axis HREM (Fig. 5b) and HAADF (Fig. 6b) images of our sample, indicating a high density of stacking faults that changes the TM (0 0 0 1) interplanar slip direction.

Different stacking sequences have been discussed as originating from several space groups ($P3_112$, $C2/m$, $C2/c$, etc.) [16,24]. However, the small size along the *c*-axis of the R and P meshes in our sample and the irregularity of the mesh sizes preclude the assignment of a single stacking sequence throughout the structure, but seem to indicate a quasi-random stacking of the TM (0 0 0 1) planes based on a $R\bar{3}m$ structure with a high density of stacking faults. This arrangement results in a pile of thin platelets, each belonging to a different space group dictated by the local plane stacking sequence,

observed in the low-magnification bright-field image (Fig. 3b). This interpretation is in agreement with the small energy differences calculated for the different local stacking sequences [24] and the $n/3$ $(1\,1\,\bar{2}\,0)$ streaks appearing in the $[1\,\bar{1}\,0\,0]$ zone-axis SAED pattern (Fig. 4b), which are characteristic of both a small ordered-domain size and lack of domain-periodicity along the c-axis (the direction of the streak). The additional broad, low intensity XRD peaks in the $20^\circ \leq 2\theta \leq 25^\circ$ range arise from the different stacking of the TM $(0\,0\,0\,1)$ planes.

Thus, the periodic contrast modulation along TM $(0\,0\,0\,1)$ planes observed in $[1\,0\,\bar{1}\,0]$ zone axis HREM (Fig. 5b) and HAADF (Fig. 6b) constitute a direct observation of the ordering of Li-substitutionals in the TM-plane, forming a $\sqrt{3} \times \sqrt{3}$ hexagonal sublattice (α-sites). However, in the $[1\,0\,\bar{1}\,0]$ projection all the α-columns look similar, showing only the average Li occupation of the α-sublattice. In order to discern whether there is additional Li-ordering within the α-sublattice, induced by Ni-substitution, one needs to consider how this idealized model structure projects along the $[1\,1\,\bar{2}\,0]$ direction. Fig. 12e and f show $[1\,1\,\bar{2}\,0]$ zone axis projections of the ordered (Fig. 12a) and disordered (Fig. 12b) Li configurations in the α-sublattice, respectively. In this projection, TM $(0\,0\,0\,1)$ planes appear as a row of atomic columns $\sqrt{3}a/2 \simeq 0.247$ nm apart, each consisting of 1/3 of α-sites and 2/3 of β-sites. This intercolumnar periodicity can be resolved in both HREM (Fig. 5a) and HAADF (Fig. 6a) images, where neighboring atomic columns appear as distinct dots $\simeq 0.247$ nm apart.

If there were Li-ion ordering within the α-sublattice, one should expect to see a contrast variation in the projected structure (Fig. 12e), as not all of the atomic columns would contain the same amount of Li; no contrast variation should be expected from the randomly occupied α-sublattice where all the atomic columns are equivalent (Fig. 12f). As no contrast variations along the TM $(0\,0\,0\,1)$ planes are apparent in either HREM (Fig. 5a) or HAADF (Fig. 6a) images, we conclude that the tendency of the Li-ion to surround itself with Mn and avoid Ni is not enough to cause an ordered Ni substitution for Li in the α-sublattice; that is, Ni substitutes for Li randomly or quasi-randomly throughout the sample.

Quasi-random substitution of Ni for Li in the α-sublattice does not necessarily preclude some degree of Ni-ion clustering in the TM $(0\,0\,0\,1)$ planes. For example, a rhombus of four Ni neighbors in the α-sublattice would enclose two β-sites devoid of Li neighbors (discontinuous green line in Fig. 12a); Ni substitution for Mn at the β-sites would then produce a Ni-ion cluster. Another possibility is the formation of $Li[Mn_{0.5}Ni_{0.5}]O_2$ building blocks, consisting of a Li atom surrounded by 6 Mn and 12 Ni atoms forming two concentric hexagonal rings, i.e., a perfectly ordered flower pattern [11]; Ni substitution for the central Li and Mn atoms would then produce a Ni cluster ($\simeq 1.5$ nm in diameter) [22]. A consequence of such Ni-clustering would be the formation of Ni-free regions, or Li_2MnO_3-like domains, in the sample [22].

In the $Li_{1.2}Ni_{0.2}Mn_{0.6}O_2$ sample, such Ni-clustering would result in a lateral variation of composition within the TM $(0\,0\,0\,1)$ planes, and display contrast variations in the $[1\,1\,\bar{2}\,0]$ zone axis TEM images; these composition and contrast variations were not observed. Additionally, EDS (Fig. 7) and EELS (Fig. 8) analyses did not show any evidence of Ni segregation, either in the grains or at grain boundaries. Ni-clusters, if they exist, are so small that any compositional variations are averaged within the probe volume ($\lesssim 10\,\text{nm}^3$). Therefore, we conclude that Ni occupation of α-sites occurs randomly and without a tendency toward elemental segregation that would result in the formation of discrete Li_2MnO_3 domains and discrete $Li(Ni_{0.5}Mn_{0.5})O_2$ domains with long-range order.

In the cycled (electrochemically activated) samples, fringe patterns were observed in most HREM images which indicate a lower degree of Li-ordering in the TM-rich layers. However, dot arrays occasionally observed in the images (see Fig. 10a) imply the presence of Li in localized areas of the TM $(0\,0\,0\,1)$ plane. The lower degree of Li-ordering is probably associated with a reduced content of Li-ions, in agreement with the observation of Armstrong et al. showing that, during $Li_{1.2}Ni_{0.2}Mn_{0.6}O_2$ charge above 4.5 V, the loss of lithium is accompanied by the loss of oxygen, resulting in an irreversible net loss of Li_2O from the structure [23]. The microscopic cracks observed in TEM images of cycled samples (see Fig. 11) are apparently the result of these material losses. The evolution of oxygen from the surface is accompanied by migration of lithium ions from the TM layers leaving vacancies that are mostly occupied by transition-metal ions diffusing from the surface into the sample bulk [23]. The presence of Li in local areas indicates that a small fraction of Li returns to the TM $(0\,0\,0\,1)$ planes on cell discharge. Similar observations were reported by Li et al. who studied the Li occupancy of TM sites in $Li(Ni_{0.5}Mn_{0.5})O_2$ samples, during and after high-voltage cycling [28].

5. Conclusions

We analyzed fresh and electrochemically activated samples of $Li_{1.2}Ni_{0.2}Mn_{0.6}O_2$ by a combination of transmission electron microscopy techniques. SAED, HREM, and HAADF imaging of the fresh sample revealed a pronounced 0.43-nm-periodic structure along $[1\,1\,\bar{2}\,0]$ directions of the basal planes in the parent $R\bar{3}m$ structure which is evidence of an in-plane $\sqrt{3} \times \sqrt{3}$ ordering of Li in the TM planes. The stacking of the Li-ordered TM $(0\,0\,0\,1)$ planes was found to be quasi-random, giving rise to platelets belonging to different crystallographic space groups. The thickness of these platelets ranges between 1 and 5 nm, as evidenced by low magnification TEM imaging. Uniform contrast in HAADF $[1\,1\,\bar{2}\,0]$ images indicates a random distribution of Li and Ni within the $\sqrt{3} \times \sqrt{3}$ sublattice. Furthermore, elemental analysis by EELS and EDS using sampling volumes $\lesssim 10\,\text{nm}^3$ revealed uniform distribution of Ni across the samples, i.e., discrete Li_2MnO_3 and $Li(Ni_{0.5}Mn_{0.5})O_2$ domains with long-range order were not observed. The electrochemically activated samples exhibited significantly weaker, although not absent, Li-ordering in TM planes. Low-magnification TEM analysis showed microscopic cracks in the activated sample, predominately along basal $(0\,0\,0\,1)$ planes, presumably due to loss of Li and O during the charging process.

Acknowledgements

This work was supported by the US Department of Energy, Office of FreedomCar and Vehicle Technologies. We acknowledge the use of the Center for Microanalysis of Materials (CMM) at the Frederick Sietz Materials Research Laboratory, University of Illinois at Urbana-Champaign (UIUC) is partially supported by the US Department of Energy under grants DE-FG02-91ER45439, DE-FG02-07ER46453 and DE-FG02-07ER46471. We thank JEOL USA, Inc. for use of the 2200FS instrument with a probe aberration corrector.

References

[1] J.-M. Tarascon, M. Armand, Nature 414 (2001) 359.
[2] D.P. Abraham, J.L. Knuth, D.W. Dees, I. Bloom, J.P. Christopherson, J. Power Sources 170 (2007) 465.
[3] Y. Makimura, T. Ohzuku, J. Power Sources 119 (2003) 156.
[4] T. Ohzuku, Y. Makimura, Chem. Lett. 30 (2001) 744.
[5] M.E. Spahr, P. Novak, B. Schnyder, O. Haas, R. Nesper, J. Electrochem. Soc. 14 (1998) 1113.
[6] Z. Lu, D.D. MacNeil, J.R. Dahn, Electrochem. Solid State Lett. 4 (2001) A191.
[7] Z. Lu, J.R. Dahn, J. Electrochem. Soc. 149 (2002) A815.
[8] J.-S. Kim, C.S. Johnson, J.T. Vaughey, M.M. Thackeray, S.A. Hackney, W.-S. Yoon, C.P. Grey, Chem. Mater. 16 (2004) 1996.
[9] Y. Koyama, Y. Makimura, I. Tanaka, H. Adachi, T. Ohzuku, J. Electrochem. Soc. 151 (2004) A1499.
[10] J. Reed, G. Ceder, Electrochem. Solid State Lett. 5 (2002) A145.
[11] A. Van der Ven, G. Ceder, Electrochem. Commun. 6 (2004) 1045.
[12] H. Kobayashi, H. Sakaebe, H. Kageyama, K. Tatsumi, Y. Arachi, T. Kamiyama, J. Mater. Chem. 13 (2003) 590.
[13] W.S. Yoon, Y. Paik, X.Q. Yang, M. Balasubramanian, J. McBreen, C.P. Grey, Electrochem. Solid State Lett. 5 (2002) A263.
[14] H. Nakano, T. Nonaka, C. Okuda, Y. Ukyo, J. Ceram. Soc. Jpn. 111 (2003) 33.
[15] Z.H. Lu, Z.H. Chen, J.R. Dahn, Chem. Mater. 15 (2003) 3214.
[16] Y.S. Meng, G. Ceder, C.P. Grey, W.S. Yoon, M. Jiang, J. Breger, Y. Shao-Horn, Chem. Mater. 17 (2005) 2386.
[17] Y.S. Meng, G. Ceder, C.P. Grey, W.S. Yoon, Y. Shao-Horn, Electrochem. Solid State Lett. 7 (2004) A155.
[18] J. Breger, Y.S. Meng, Y. Hinuma, S. Kumar, K. Kang, Y. Shao-Horn, G. Ceder, C.P. Grey, Chem. Mater. 18 (2006) 4768.
[19] W.S. Yoon, S. Iannopollo, C.P. Grey, D. Carlier, J. Gorman, J. Reed, G. Ceder, Electrochem. Solid State Lett. 7 (2004) A167.
[20] C.S. Johnson, J.-S. Kim, C. Lefief, N. Li, J.T. Vaughey, M.M. Thackeray, Electrochem. Commun. 6 (2004) 1085.
[21] M.M. Thackeray, S.-H. Kang, C.S. Johnson, J.T. Vaughey, S.A. Hackney, Electrochem. Commun. 8 (2006) 1531.
[22] M.M. Thackeray, S.-H. Kang, C.S. Johnson, J.T. Vaughey, R. Benedek, S.A. Hackney, J. Mater. Chem. 17 (2007) 3112.
[23] A.R. Armstrong, P. Holzapfel, P. Novak, C.S. Johnson, S.-H. Kang, M.M. Thackeray, P.G. Bruce, J. Am. Chem. Soc. 128 (2006) 8694.
[24] J. Breger, M. Jiang, N. Dupreĭ, Y.S. Meng, Y. Shao-Horn, G. Ceder, C.P. Grey, J. Solid State Chem. 178 (2005) 2575.
[25] S. Miao, M. Kocher, P. Rez, B. Fultz, Y. Ozawa, R. Yazami, C.C. Ahn, J. Phys. Chem. B 109 (2005) 23473.
[26] W.S. Yoon, M. Balasubramanian, K.Y. Chung, X.Q. Yang, J. McBreen, C.P. Grey, D.A. Fischer, J. Am. Chem. Soc. 127 (2005) 17479.
[27] W.S. Yoon, M. Balasubramanian, X.Q. Yang, Z. Fu, D.A. Fischer, J. McBreen, J. Electrochem. Soc. 151 (2004) A246.
[28] H.H. Li, N. Yabuuchi, Y.S. Meng, S. Kumar, J. Breger, C.P. Grey, Y.S. Horn, Chem. Mater. 19 (2007) 2551.
[29] N. Yabuuchi, S. Kumar, H.H. Li, Y.-T. Kim, Y.S. Horn, J. Electrochem. Soc. 154 (2007) A566.
[30] S.-H. Kang, Y.-K. Sun, K. Amine, Electrochem. Solid State Lett. 6 (2003) A183.